nature materials

ARTICLES

https://doi.org/10.1038/s41563-021-01042-y

Check for updates

Microenvironment-triggered multimodal precision diagnostics

Liangliang Hao[1,2], Nazanin Rohani[1], Renee T. Zhao[2], Emilia M. Pulver[2], Howard Mak[1], Olivia J. Kelada[3], Henry Ko[1,2], Heather E. Fleming[1,4], Frank B. Gertler[1,5] and Sangeeta N. Bhatia[1,2,4,6,7,8,9] ✉

Therapeutic outcomes in oncology may be aided by precision diagnostics that offer early detection, localization and the opportunity to monitor response to therapy. Here, we report a multimodal nanosensor engineered to target tumours through acidosis, respond to proteases in the microenvironment to release urinary reporters and (optionally) carry positron emission tomography probes to enable localization of primary and metastatic cancers in mouse models of colorectal cancer. We present a paradigm wherein this multimodal sensor can be employed longitudinally to assess burden of disease non-invasively, including tumour progression and response to chemotherapy. Specifically, we showed that acidosis-mediated tumour insertion enhanced on-target release of matrix metalloproteinase-responsive reporters in urine. Subsequent on-demand loading of the radiotracer ^{64}Cu allowed pH-dependent tumour visualization, enabling enriched microenvironmental characterization when compared with the conventional metabolic tracer ^{18}F-fluorodeoxyglucose. Through tailored target specificities, this modular platform has the capacity to be engineered as a pan-cancer test that may guide treatment decisions for numerous tumour types.

Precision diagnostics that provide actionable information on the presence, progression and treatment response of disease are essential for improving oncology outcomes[1]. Current diagnostic strategies rely on a combination of imaging tests and molecular diagnostic assays to monitor endogenous biomarkers[2,3]. Imaging tests, such as computed tomography (CT) for lung cancer, remain the clinical standard for detection and localization of disease; however, these methods suffer from poor specificity when employed in a screening paradigm, and can lead to invasive follow-up procedures with risk of complications[4]. Recent advances in molecular diagnostics have yielded promising assays to measure alternative endogenous disease biomarkers, including blood tests that detect somatic mutations ('liquid biopsy'), multi-analyte circulating tumour DNA and protein biomarkers ('CancerSEEK'), that have the potential to identify the tissue of origin[5–7]. Although molecular characterization of mutational heterogeneity offers the capacity for high specificity, strategies that detect circulating endogenous biomarkers face intrinsic sensitivity limitations for early-stage disease and necessitate diagnostic imaging to confirm and localize the disease in a prospective manner[8–11]. Recognizing that surgery can be curative for many localized solid tumours, a push to develop multimodal tools that couple sensitive, early cancer detection with specific localization is emerging to inform cancer care[12,13].

To overcome the limitations faced by conventional imaging tests and endogenous biomarkers, and with an eye towards designing a future pan-cancer detection tool, we engineered a multimodal material within the new paradigm of synthetic biomarkers for molecular diagnostics: to induce a signal that did not previously exist in the body[8,14–16]. These exogenously administered synthetic biomarkers are selectively activated in the tumour microenvironment to shed reporters into biofluids, and have been shown previously to achieve high-sensitivity detection of tumours in vivo[9,16–18]. As the synthetic biomarker field matures, the focus is shifting to determine how to use these tests to intervene in cancer progression and treatment responses. To close the gap on their clinical actionability, in this study we engineered protease-responsive imaging sensors for malignancy (PRISM) to combine the delivery of activity-driven synthetic biomarkers with the capacity to be 'loaded on-demand' to create a positron emission tomography-computed tomography (PET-CT) imaging agent for both in situ and non-invasive disease visualization and monitoring.

This modular material platform leverages the coexisting, generalizable hallmarks of invasive tumours, that is, aberrant proteolytic activity and increased extracellular acidification at the invasive tumour front, to enhance the specificity of its diagnostic signal[19,20]. We exploited a pan-cancer molecular signature, matrix metallopeptidase 9 (MMP9), which turns on the angiogenic switch and has previously been validated to be more sensitive than circulating free DNA in mouse models[9,17,21]. Positive MMP9-derived urinary tests were sequentially confirmed by a diagnostic PET-CT, which precisely localizes the tumour nodules in a way that a molecular predictor of tissue-of-origin cannot[3,6]. We benchmarked tumour acidosis-mediated imaging against a conventional metabolic tracer, and demonstrated longitudinal monitoring of cancer progression and regression in two disseminated colorectal cancer (CRC) models treated with a first-line clinical chemotherapy regimen[22]. Providing both tools in a single modality shortens the regulatory path to patients, and yields an actionable resource with the capacity to inform clinicians on their next interventional steps during monitoring for drug response or relapse. In addition to CRC, the PRISM platform is positioned to be refined as a precision diagnostic for other cancer types by exploiting enzymatic signatures in

[1]Koch Institute for Integrative Cancer Research, Massachusetts Institute of Technology, Cambridge, MA, USA. [2]Institute for Medical Engineering and Science, Massachusetts Institute of Technology, Cambridge, MA, USA. [3]Preclinical Imaging, PerkinElmer, Hopkinton, MA, USA. [4]Howard Hughes Medical Institute, Cambridge, MA, USA. [5]Department of Biology, Massachusetts Institute of Technology, Cambridge, MA, USA. [6]Department of Electrical Engineering and Computer Science, Massachusetts Institute of Technology, Cambridge, MA, USA. [7]Department of Medicine, Brigham and Women's Hospital and Harvard Medical School, Boston, MA, USA. [8]Broad Institute of Massachusetts Institute of Technology and Harvard, Cambridge, MA, USA. [9]Ludwig Center at Massachusetts Institute of Technology's Koch Institute for Integrative Cancer Research, Cambridge, MA, USA. ✉e-mail: sbhatia@mit.edu

a range of disease microenvironments and across a diverse set of oncogenic drivers.

Nanosensors localize in invasive CRC through tumour acidosis

The tumour microenvironment (TME) plays an essential role in promoting local invasion and distant metastasis across many types of cancer. On this basis, we elected to engineer a versatile multimodal nanosensor that leverages tumour-specific extracellular molecular activities and, in so doing, develop a single tool for use in both precision diagnosis and treatment monitoring. For the primary function, we harnessed the presence of acidosis in the TME using a pH low insertion peptide (pHLIP) attached to a polychain polyethylene glycol (eight-arm PEG, 40 kDa) polymeric scaffold by click chemistry. This peptide was designed to enable active tumour trafficking of the nanosensor, as pHLIP-mediated extravasation and intracellular insertion are triggered by a peptide conformational switch upon acidification in both primary tumours and metastatic lesions (Fig. 1a, Supplementary Figs. 1 and 2, and Table 1)[23]. Such membrane affinity and the cooperativity of the transition to the membrane-inserted state can be enhanced through an increase in the valency of the peptide display, and inhibited by modification of negatively charged residues (Asp or Glu; Supplementary Fig. 1)[24]. To track the nanosensor trafficking to disseminated tumours through a pH switch, we established a transplantation CRC model through intravenous injection of a metastatic murine CRC line (MC26-LucF) in female BALB/c mice[17,25,26]. Three weeks after tumour inoculation, we performed high-throughput cryo-fluorescence tomography (CFT) on whole animals after systemic administration of fluorescein amidite (FAM)-labelled PRISM, and observed the localization of the fluorescent signal in a pattern that was perfectly aligned with the corresponding anatomical tumours that had formed throughout the lung (Fig. 1b and Supplementary Fig. 3a,b). Using conventional tumour section immunofluorescence, CRC lung nodules exhibited PRISM localization concentrated at the tumour periphery, and colocalized with expression of a key extracellular matrix (ECM) regulator, MMP9 (Fig. 1c). Greater than 80% of the detected MMP9 protein expression overlapped with FAM-staining, which marks PRISM in the tumour (Fig. 1c and Supplementary Fig. 3c,d).

Microenvironmental acidification is thought to regulate the metastatic potential of tumour and stromal cells through alteration of metabolic reprogramming, angiogenesis, immune suppression and therapeutic resistance[27–30]. This effect may be in part due to acidosis-driven signals that enhance the expression of proteases, the activity of which break down the ECM and promote tumour invasion[31]. The Cancer Genome Atlas (TCGA) dataset queries revealed that carbonic anhydrase 9 (CAIX), a major proton transporter that contributes to extracellular acidification[31–33], was overexpressed in human tumours from many tissues (Supplementary Fig. 4a). Staining of CRC tissue microarray (TMA) samples revealed consistent elevation of CAIX protein expression in tumour sections relative to normal human tissue (Fig. 1d and Supplementary Fig. 5a,c). Consistent with what our group has observed in lung, prostate and ovarian tumours[17,18], analysis of the transcriptomic patterns of two carcinomas (breast invasive carcinoma, BRCA, and colon adenocarcinoma, COAD) and one blastoma (glioblastoma multiforme, GBM) revealed that several collagen-degrading matrix metalloproteinases (MMPs) as well as ECM components that stimulate cancer cell invasion were also upregulated in CRC (Supplementary Fig. 4b). Notably, when this human sample data were used to test the hypothesis that gene expression could be predictive in disease detection using a receiver operating characteristic (ROC) curve analysis, we observed that although MMP9 expression was moderately diagnostic (area under the ROC curve, AUC = 0.683), the combination of MMP9 with CAIX could strongly distinguish tumour samples from controls (AUC = 0.946; Fig. 1e).

In light of the diagnostic power enhancement achieved by combining two ubiquitous hallmarks of cancer, the second TME-based addition to PRISM was an engineered peptide substrate that samples CRC-associated MMP9 activity and releases ligand-encoded reporters into the urine through size-specific kidney concentration. The proteolytic signature of MMP9 turns on the angiogenic switch, even at the earliest stages of tumorigenesis. Elevated MMP9 levels were validated in CRC mouse models and human COAD biopsies (Supplementary Fig. 5b–d). We first tested the cleavage kinetics of several reported MMP substrates, and selected one (PLGVRGK) with optimized MMP9 specificity using fluorescence resonance energy transfer (FRET)-based fluorometric peptide substrate cleavage assays with purified MMP9 enzyme and lysates from tumour tissue samples (Supplementary Fig. 6). We then linked the affinity-tagged MMP9-responsive peptide to the polymeric core, which was additionally functionalised through direct linkages to the pHLIP peptide or its non-targeting counterpart (Supplementary Fig. 7a). The resulting PRISM or control sensors showed a uniform spherical shape and similar sizes (23.93 ± 3 and 35.9 ± 10 nm) in cryogenic transmission electron microscopy (Cryo-TEM; Supplementary Fig. 7b,c). Both types of sensors tolerated the click conjugation of the azide-terminated MMP9-activated reporter, pHLIP (or its non-targeting control peptide) and PEG with dibenzocyclooctyne (DBCO), yielding monodisperse nanoparticles with equal stoichiometric loading (Supplementary Fig. 7d–f). The conjugation of PEG caused an increase in the hydrodynamic diameter (Supplementary Fig. 7e). When incubated with multiple human and murine cancer cells at acidic pH (6.4) in vitro, PRISM exhibited significantly higher cellular accumulation than at physiological pH (7.4) (Supplementary Fig. 8).

Multimodal monitoring of lung metastases with PRISM

After characterizing the TME-directed nanosensors, we assayed whether they could detect tumour lesions that are notoriously challenging to detect: lung tumours[34]. In conventional medical imaging such as PET, lung tumour signals are often masked by the dramatic uptake of the glucose analogue ^{18}F-fluorodeoxyglucose (^{18}F-FDG) by metabolically active cardiac cells[35]. Furthermore, the false positive detection rate of clinical lung masses is high, due to the prevalence of accumulated scar tissue and other benign structures that can appear indistinguishable from malignant and growing lung lesions. To enable PET-based imaging through isotope-loaded PRISM, we site-specifically labelled pHLIP with the mono-maleimide-bearing metal chelator 1,4,7-triazacyclononane-1,4-bis-acetic acid-7-maleimidoethylacetamide (maleimide-NOTA) to bind the positron-emitting radionuclide (^{64}Cu, $t_{1/2} = 12.701 \pm 0.002$ h) to generate ^{64}Cu-labelled PRISM (^{64}Cu-PRISM; Fig. 2a and Supplementary Fig. 2). Based on the discriminatory power of targeting tumour acidosis (Fig. 1b and Supplementary Figs. 3a and 8), we hypothesized that PRISM could optimize the PET signal by promoting longer in vivo circulation times and enhanced tumour-homing through the multivalent orientation of pHLIP. We then validated the efficacy of the ^{64}Cu-PRISM in the aforementioned CRC lung tumour model, in which lung nodule formation was observed within 2–3 weeks of systemic inoculation of tumour cells (Fig. 2b).

Upon intravenous administration of nanosensors, urine samples from tumour-bearing and healthy control mice were collected after 1 h, and the enzyme-linked immunosorbent assay (ELISA) read-outs of protease-liberated reporter levels increased as tumour growth progressed (Fig. 2a,c). Ex vivo fluorescence scanning, histological and Immunofluorescence analyses of PRISM distribution in the tumour-bearing and healthy lung tissues revealed tumour-specific sensor accumulation, suggesting that the pH-selective targeting of PRISM through pHLIP enhanced on-target MMP9 cleavage (Supplementary Figs. 9a,c–e and 10). Furthermore, in the same mice that exhibited significant elevation of the MMP-dependent urine

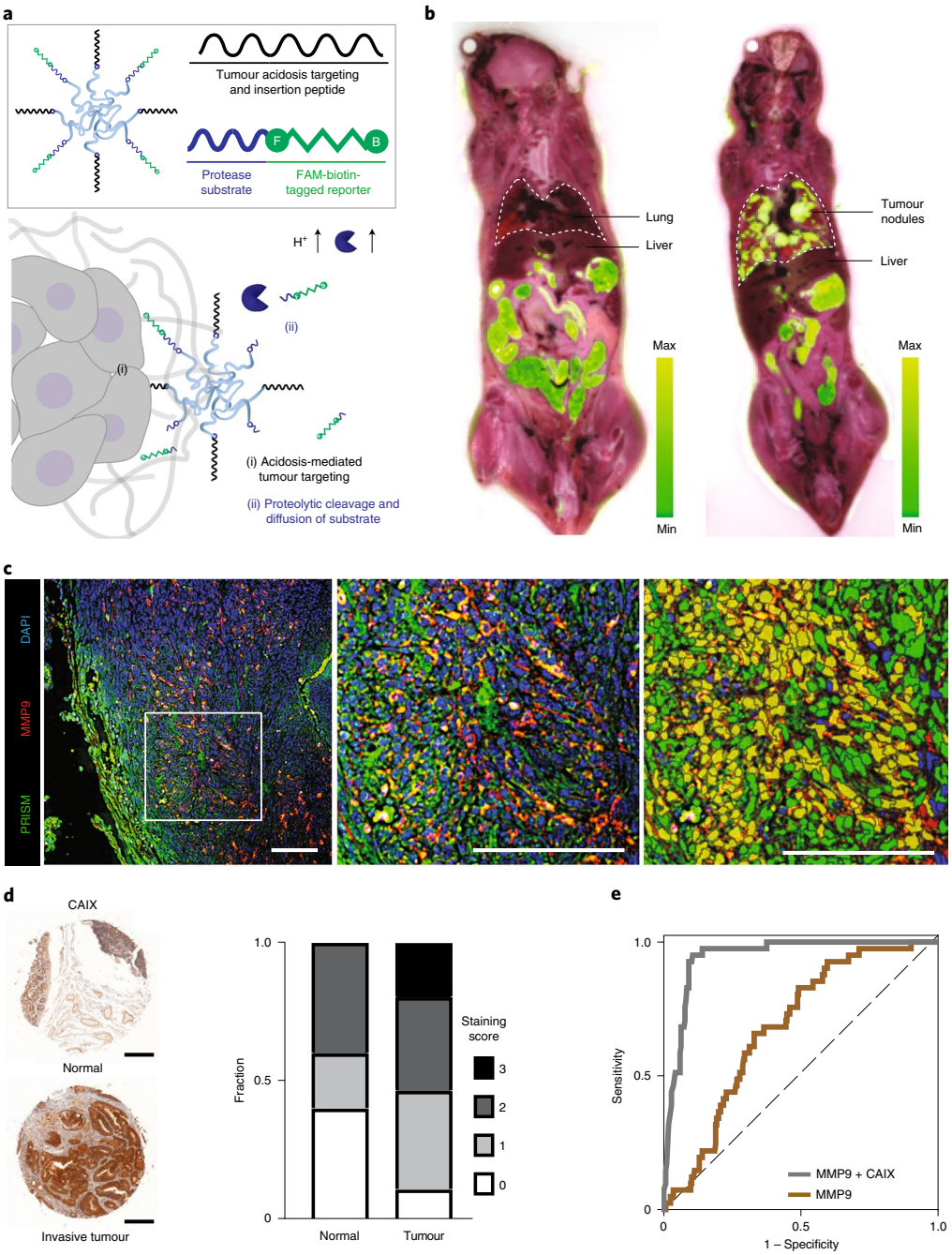

Fig. 1 | Targeting multivalent nanosensors to invasive CRC through tumour acidosis. a, Design of PRISM that targets cancer cells in the acidic TME. Acidosis-mediated tumour insertion enables cancer-specific targeting and imaging (i). Activation of PRISM by tumour-specific protease activity triggers release of a synthetic reporter that can partition into urine for non-invasive detection (ii). The blue 3/4 circles represent the disease-associated proteases. F, FAM; B, biotin. **b**, CFT of healthy BALB/c mouse (left) and mouse with lung tumours (right) 6 h after PRISM administration. The images represent individual 25 μm sections from the cryo-macrotome and depict the overlay of bright-and-white organ sectioning with FAM fluorescence from PRISM in the tissue sections. The colour scales show fluorescence intensity in arbitrary units. **c**, Colocalization analysis of MMP9 immunofluorescence (red) and PRISM-labelled acidic areas (green) in tumour lesions of lung sections. Left, immunofluorescence staining of a typical tumour-bearing lung section; middle, zoom-in view of the left image; right, cell-based segmentation analysis of the middle image. The numbers of MMP9-positive and PRISM-positive cells were quantified in three sections. Cell-based overlap and Pearson correlation coefficient analysis of 1,276 cells indicated 83.1% of the MMP9-positive cells overlapped with FAM-staining of the PRISM-positive cells in the tumour. Scale bars, 100 μm. Immunofluorescence staining was completed independently three times by different investigators with similar results. DAPI (4′,6-diamidino-2-phenylindole) stained the nuclei in blue. **d**, Representative immunohistochemistry staining and blind expression scores of CAIX protein levels in patient tissue microarrays of normal colon and colon adenocarcinoma biopsies. The IHC staining intensity was blindly scored by a pathologist and assigned according to the scale as 0 (negative, no visible staining), 1 (weakly positive, pale yellow), 2 (moderate positive, yellow), and 3 (strongly positive, dark brownish-yellow). Scale bars, 500 μm. Full TMA staining is shown in Supplementary Fig. 5. Staining was completed twice with similar results. **e**, ROC curves constructed on the basis of the messenger RNA level of MMP9 solely (AUC = 0.683) or of dual analytes (MMP9 and CAIX; AUC = 0.946), showing cancer classification as distinct from normal tissue. The dashed line represents a purely random diagnostic tool with an AUC value of 0.5.

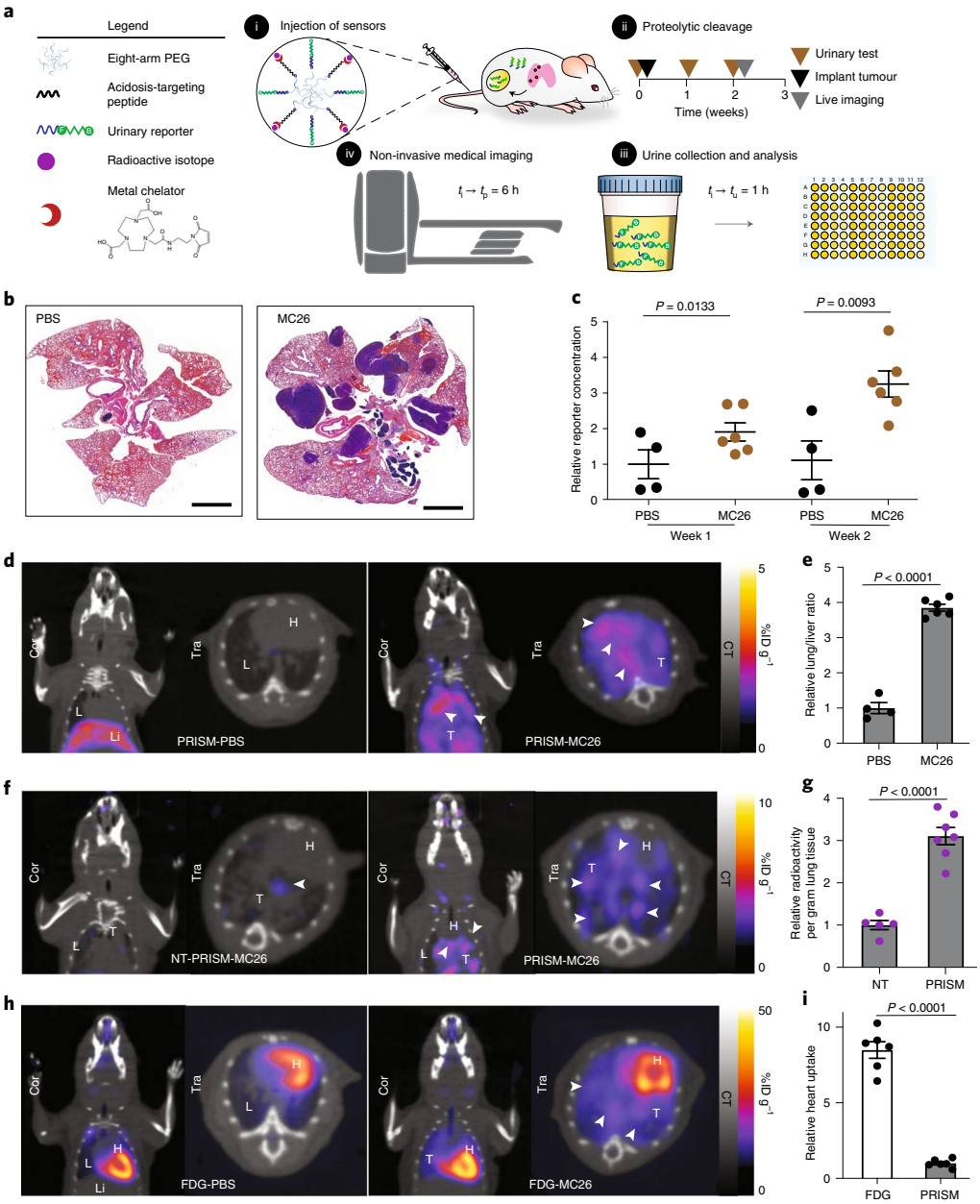

Fig. 2 | Positron-emitting radionuclide-loaded ^{64}Cu-PRISM achieved multimodal monitoring of CRC lung nodules. a, Schematic showing the functional moieties, that is, the tumour-targeting peptide, protease substrate and imaging tracers displayed on a nanosensor surface (i), study time course of tumour transplantation (ii), urinary testing and analysis (iii) and PET-CT imaging (iv) in a syngeneic CRC pulmonary disease model. t_i, time of sensor injection; t_p, time of PET/CT imaging; t_u, time of urine collection. **b**, Representative histological images of lungs from healthy (left) and CRC tumour-bearing (right) BALB/c mice on day 17 after tumour inoculation. Scale bars, 2 mm. PBS, phosphate-buffered saline. Experiments were completed independently three times with similar results. **c**, Relative reporter concentrations measured in the urine of healthy mice ($n = 4$ mice per group) versus CRC lung tumour-bearing mice ($n = 6$ mice per group) after application of PRISM (data are represented as mean ± s.e.m.; unpaired two-tailed t-test with Welch's correction). **d**, PET-CT images of healthy and tumour-bearing mouse lungs at week 2, 6 h after administration of ^{64}Cu-PRISM, showing coronal (Cor) and transverse (Tra) views. The arrowheads show the presence of CRC lung tumours. L, lung; Li, liver; H, heart; T, tumour nodules. The units %ID g^{-1} represent the percentage of injected radioactive dose per gram of tissue. **e**, Quantification of the representative images in **d** showing an elevated lung-to-liver ratio in the lung tumour-bearing mice (MC26; $n = 6$ mice per group) compared with the healthy control mice (PBS; $n = 4$ mice per group; data are shown as mean ± s.e.m., normalized to the healthy control animal; unpaired two-tailed t-test with Welch's correction). **f**, Representative PET-CT images of the lung in animals imaged with ^{64}Cu-non-targeting (NT)-PRISM (left) or ^{64}Cu-PRISM (right). The arrowheads mark the presence of CRC lung tumours. L, lung; H, heart; T, tumour nodules. **g**, Ex vivo quantification of the radioactivity accumulated in the lungs extracted from animals imaged with ^{64}Cu-NT-PRISM (NT; $n = 5$ mice per group) or ^{64}Cu-PRISM (PRISM; $n = 7$ mice per group), represented as ^{64}Cu counts per minute per gram tissue (data are represented as mean ± s.e.m.; unpaired two-tailed t-test with Welch's correction). **h**, ^{18}F-FDG PET-CT scans of the same healthy and tumour-bearing mice as in **d** 1 h after tracer injection showing signal accumulation from active glucose uptake. L, lung; Li, liver; H, heart; T, tumour nodules. The arrowheads in **h** mark the presence of CRC lung tumours. **i**, Quantification of the images in **d** and **h** indicating a significantly lower background in the chest when lung tumour-bearing animals are imaged with PRISM compared with the conventional ^{18}F-FDG tracer (data are shown as mean ± s.e.m., normalized to the tumour-bearing animal imaged with PRISM; unpaired two-tailed t-test with Welch's correction).

signal at the 2-week time point, PET-CT imaging using ^{64}Cu-loaded PRISM localized CRC lung tumours, resulting in substantially increased positive-to-negative tumour ratios (3.85 ± 0.25; Fig. 2d,e and Supplementary Table 2). Consistent with the fluorescent read-out (Supplementary Fig. 10), such tumour-specific PET signals were not observed in animals injected with non-acidosis-targeting control nanosensors, as verified by the 3.11 ± 0.23-fold tracer accumulation in the tumour-bearing lungs exposed to ^{64}Cu-PRISM relative to the signal derived from the control sensor (Fig. 2f,g). Importantly, we re-imaged the same mice shown in Fig. 2d using PET-CT with the conventional PET tracer used in clinics, ^{18}F-FDG, and compared the results with those obtained by imaging with ^{64}Cu-PRISM. Although the standard uptake value remained comparable when imaging the lung, ^{18}F-FDG exhibited a strong accumulation in the heart, and the resulting high background signal obscures some of the lung-derived signal that is visible in ^{64}Cu-PRISM-derived images, which gave rise to significantly less background signal in the chest (Fig. 2h,i). Notably, we observed no adverse effects in the kidney or liver following repeated administration of the PRISM nanosensors in these immunocompetent hosts, as reflected by the normal histological staining and clearance kinetics (Supplementary Fig. 11). Therefore, PRISM offers great potential in detecting tumours in the lung.

Longitudinal, multimodal monitoring of CRC liver nodules

Following multimodal monitoring of tumour progression in the lung, we next evaluated the efficacy of the PRISM platform in the liver, another organ that has also been clinically challenging to image due to its elevated background uptake[36]. Clinically, CRC primarily migrates to the liver, and this process can be surgically induced in mice through intrasplenic injection of the CRC cell line. This procedure exhibited robust tumour penetrance, such that 70–80% of immunocompetent BALB/c mice formed liver nodules within 2 weeks of injection of MC26-LucF, allowing for total burden monitoring by bioluminescence imaging (Fig. 3a and Supplementary Fig. 12a,b). At this time point, PRISM particles were systemically administered to both control and tumour-bearing mice. Prior to urine analysis, the mice underwent fluorescent imaging, which revealed that the PRISM particles specifically accumulated in CRC nodules in diseased liver (Supplementary Fig. 12c). Urine samples were collected 1 h after sensor injection and the protease-liberated reporter levels were detected by the ELISA assay. Consistent with the lung tumour results, the urinary signals were significantly elevated in the tumour-bearing animals, relative to the healthy controls (Fig. 3b). Moreover, when the nanosensors incorporated a non-targeting counterpart of pHLIP, the tumour-specific signal was dampened almost twofold, suggesting that the pH-selective targeting of PRISM enhanced the sensitivity of detection (Fig. 3b). These observations aligned with the in vivo and ex vivo overlap of tumour and pHLIP-containing PRISM but not with the control NT-PRISM (Supplementary Fig. 12c,d). The tumours were allowed to progress for an additional 2 weeks, after which ^{64}Cu-PRISM particles were re-administered, and following both urine testing and live imaging, the mice were sacrificed and their livers were subjected to ex vivo immunofluorescent histochemistry. MMP9 staining was elevated in the liver tumours and largely colocalized with FAM-staining, which marks PRISM probes (Fig. 3c). Quantitatively, greater than 60% of MMP9 expression overlapped with PRISM-positive cells in acidic areas close to the tumour/stroma interface, where the hallmarks of tumour invasion are enriched (Fig. 3c and Supplementary Fig. 12e).

In addition to urine-based detection by means of PRISM, we evaluated whether PRISM could track tumour progression using PET-CT imaging. In tumour-bearing animals 2 weeks post-splenectomy, PET-CT imaging 6 h post-intravenous injection of ^{64}Cu-PRISM (and 5 h post-urine collection) showed bright illumination of CRC liver tumours that were particularly enriched at the invasive front at the tumour/stroma interfaces (Fig. 3d). Tissue uptake of ^{64}Cu-PRISM was measured in the tumours and surrounding liver tissue, resulting in positive-to-negative tumour ratios of 2.2:1 (Fig. 3d,f,g). We also found that the radioactivity uptake values in major organs, such as the liver, kidney, lung and intestine, were comparable in the same tumour-bearing mice sequentially imaged with ^{64}Cu-PRISM or ^{18}F-FDG (Fig. 3e) suggesting that ^{64}Cu-PRISM is at least as sensitive as conventional reagents. In addition, when PRISM was used to perform longitudinal tracking of tumour progression in individual animals, the ^{64}Cu-PRISM PET measurement of liver tumour expansion (Fig. 3f) matched a corresponding increase in MMP9-cleavable reporter signals over time (Fig. 3g). An important clinical limitation of ^{18}F-FDG-based PET imaging is its dependence on high glucose uptake by the target cells. In contrast, tumours derived from the human CRC line with low glucose uptake (LS 174T)[37] demonstrated an 8.6-fold tracer uptake over the surrounding normal muscles when ^{64}Cu-PRISM was used, whereas the tumour uptake of ^{18}F-FDG was indistinguishable from the background tissue (Supplementary Fig. 13).

Non-invasive assessment of tumour response to therapy

Although a large proportion of CRC patients experience liver or lung metastases, the predominant intervention used for patients

Fig. 3 | PRISM-enabled longitudinal, multimodal monitoring and imaging of CRC liver nodules. a, Left, schematic showing PRISM-carrying radioactive PET-CT tracer tested in a syngeneic model of CRC hepatic invasion for urinary detection and imaging capabilities, as well as the study time course of tumour transplantation, urinary testing and PET-CT imaging. Right, representative IVIS image for luminescence of Balb/c mouse 16 days post intrasplenic injection of MC26-LucF. Liver tumour formation was confirmed by bioluminescence imaging of tumour-bearing mice over time ($n = 10$ mice; data are shown as mean ± s.e.m.). **b**, Relative reporter concentrations in urine samples 1 h after administration of PRISM and its untargeted counterpart in healthy (PBS) and tumour-bearing mice (MC26; $n = 5$ mice per group; data are represented as mean ± s.e.m.; unpaired two-tailed *t*-test with Welch's correction). **c**, Colocalization analysis of MMP9 immunofluorescence (red) and PRISM-labelled acidic areas (green) in tumour lesions of liver sections. Left, immunofluorescence staining of a typical tumour-bearing liver section; middle, zoom-in view of the left image; right, cell-based segmentation analysis of the middle image. The numbers of MMP9-positive and PRISM-positive cells were quantified in three sections. Of the 1,130 cells quantified, 60.4% of the MMP9-positive cells overlapped with the PRISM-localized cells in the tumour (Supplementary Fig. 12e). DAPI stained the nuclei in blue. Scale bars, 100 µm. **d**, Representative maximum intensity projections (MIPs) of CRC liver tumour-bearing mice following administration of ^{18}F-FDG (i) and ^{64}Cu-PRISM (ii) 2 days later. Arrowheads in **d** and **f** mark the presence of CRC liver tumours. H, heart; T, tumour nodules; K, kidneys; I, intestines; B, bladder. **e**, Quantitative analysis of the key organs, that is, the liver, kidney, heart, lung, intestine and muscle, in tumour-bearing mice imaged with ^{18}F-FDG and ^{64}Cu-PRISM during disease progression ($n = 3$ mice per group; data are shown as mean ± s.d.; unpaired two-tailed *t*-test with Welch's correction). **f**, Transverse (Tra) views of liver nodules in tumour-bearing animals imaged longitudinally 2 and 4 weeks (wks) after tumour inoculation. The colour scale shows the percentage of injected radioactive dose per gram of tissue (units %ID g^{-1}). Scale from 0 (minimum) to 12 (maximum). **g**, Longitudinal, multimodal monitoring of the urinary reporter level and positive-to-negative tumour ratios in the liver quantified by PET-CT imaging 2 and 4 weeks after tumour inoculation ($n = 5$ mice per group for the urinary reporter level; data are shown as mean ± s.e.m.; Kolmogorov–Smirnov test for normal distribution followed by Brown–Forsythe and Welch analysis of variance (ANOVA) test with Dunnett's T3 multiple comparisons; $n = 3$ mice per group for PET imaging 2 and 4 weeks post-tumour inoculation; the data are represented as mean ± s.d.).

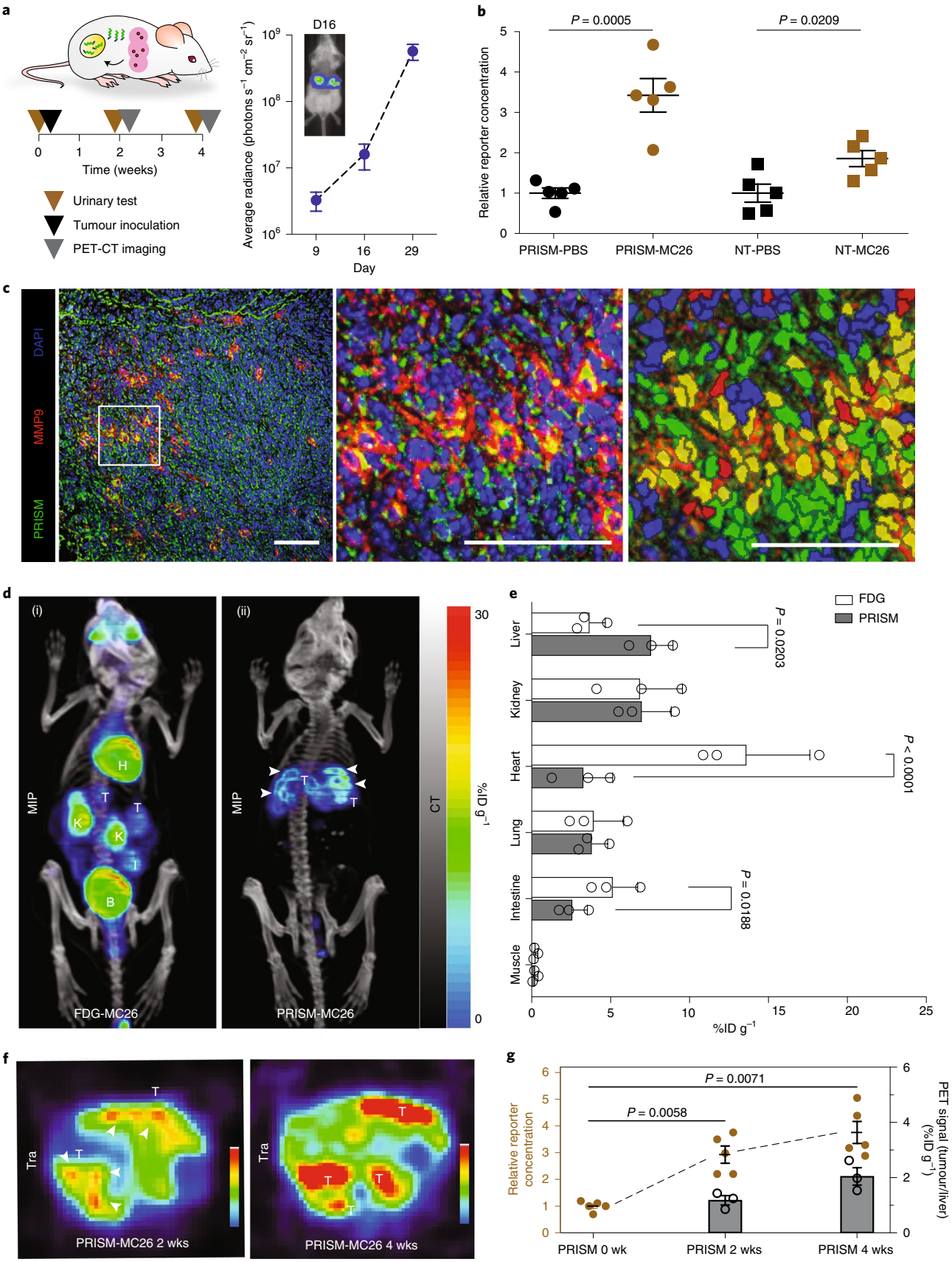
a
Time (weeks)
Urinary test
Tumour inoculation
PET-CT imaging
D16
Average radiance (photons s−1 cm−2 sr−1)
Day
b
P = 0.0005
P = 0.0209
Relative reporter concentration
PRISM-PBS
PRISM-MC26
NT-PBS
NT-MC26
c
DAPI
MMP9
PRISM
d
(i)
(ii)
MIP
FDG-MC26
PRISM-MC26
CT
%ID g−1
e
FDG
PRISM
Liver
Kidney
Heart
Lung
Intestine
Muscle
P = 0.0203
P < 0.0001
P = 0.0188
%ID g−1
f
Tra
PRISM-MC26 2 wks
PRISM-MC26 4 wks
g
P = 0.0071
P = 0.0058
Relative reporter concentration
PET signal (tumour/liver) (%ID g−1)
PRISM 0 wk
PRISM 2 wks
PRISM 4 wks

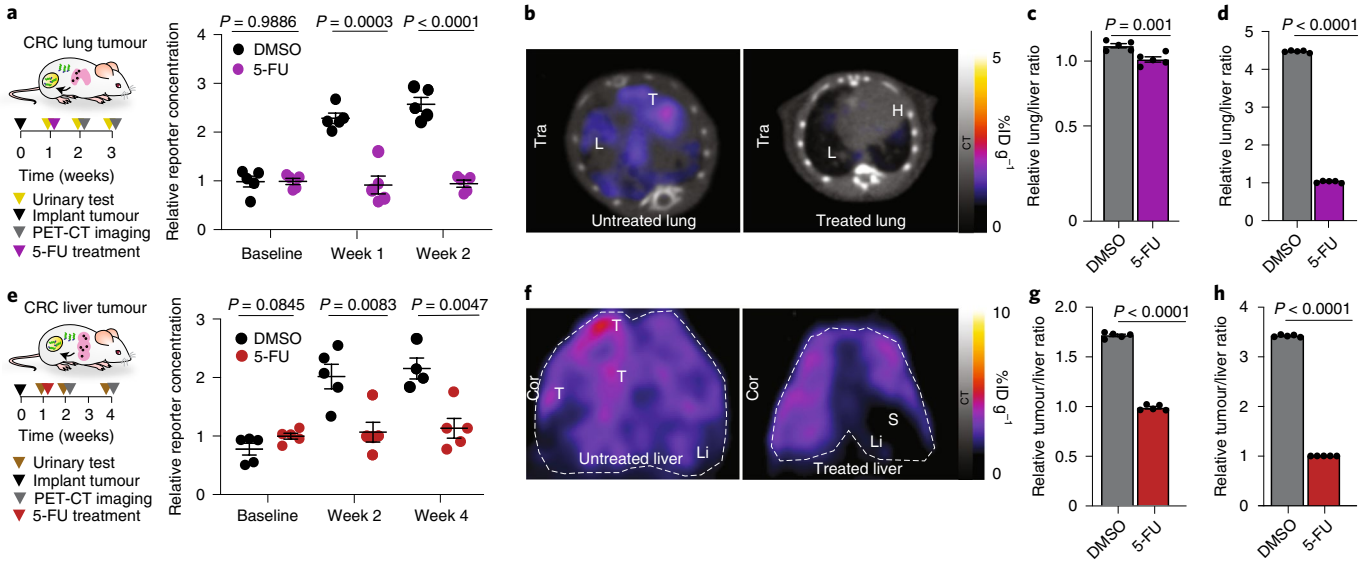

Fig. 4 | Non-invasive multimodal monitoring of the therapeutic response to a first-line chemotherapeutic by PRISM. a, Schematic of drug treatment monitoring testing in the aforementioned CRC lung metastasis model. Mice were divided into two categories: one group received the vehicle control (dimethylsulfoxide, DMSO) in PBS, the other received 5-FU at 15 mg per kg in PBS. The mice were chosen to balance a similar range of tumour burden between the groups. Also shown is the plot of the relative reporter concentrations measured in the urine of lung tumour-bearing mice with or without 5-FU treatment ($n=5$ mice per group; data are represented as mean ± s.e.m., mean normalized to 5-FU-treated mice; unpaired two-tailed *t*-test with Welch's correction; not significant, $P=0.9886$ for baseline). **b**, PET-CT transverse (Tra) views of tumour progression after 2 weeks of 5-FU treatment in mice with CRC lung tumours compared with untreated mice. T, tumour nodules; H, heart; L, lung. **c**,**d**, Relative lung-to-liver ratios quantified from the longitudinal PET-CT images collected after 1 (**c**) or 2 weeks (**d**) of 5-FU treatment in mice with CRC lung tumours compared with untreated mice (data are shown as mean ± s.e.m., mean normalized to 5-FU-treated mice; unpaired two-tailed *t*-test with Welch's correction; $n=5$ mice per group). **e**, Schematic of drug treatment monitoring testing in the CRC liver metastasis model. The untreated group received the vehicle DMSO in PBS, and the treated group received 5-FU at 15 mg per kg in PBS. Also shown is a plot of the relative reporter concentrations measured in the urine of liver tumour-bearing mice with or without 5-FU treatment ($n=5$ mice per group; data are represented as mean ± s.e.m., mean normalized to 5-FU-treated mice; unpaired two-tailed *t*-test with Welch's correction; not significant, $P=0.0845$ for baseline). **f**, Coronal (Cor) views of PET-CT images of tumour progression after 3 weeks of 5-FU treatment in mice with CRC liver tumours compared with untreated mice. T, tumour nodules; Li, liver; S, stomach. **g**,**h**, Relative positive-to-negative tumour ratios in the liver were quantified from the longitudinal PET-CT images collected after 1 (**g**) or 3 weeks (**h**) of vehicle or drug treatment in the untreated and 5-FU treated cohorts, respectively ($n=5$ mice per group; data are represented as mean ± s.e.m., mean normalized to 5-FU-treated mice; unpaired two-tailed *t*-test with Welch's correction).

with this diagnosis remains treatment with 5-fluorouracil (5-FU)/leucovorin, a standard chemotherapy. During the course of treatment, non-invasive response monitoring is essential to screen for tumour recurrence after surgical resection and to derive individualized assessment of drug–target interactions and subsequent efficacy. Therefore, we employed PRISM to monitor the local extracellular activities of tumours during drug treatment. We divided cohorts of either lung or liver CRC tumour-bearing BALB/c mice into experimental groups that received a course of 5-FU treatment and control groups that received only vehicle (Fig. 4a,e). The disseminated lung tumour model is a more rapidly progressing disease, and so these animals were followed for a total of 2 weeks (Fig. 4a–d), whereas the liver CRC-bearing mice were monitored for 4 weeks (Fig. 4e–h). PRISM sensors were administered to each group at the beginning of the 5-FU treatment, and then weekly thereafter. With each administration, urinary reporter concentration was assayed 1 h after intravenous injection of the nanosensors, providing a read-out of in vivo proteolytic activity, which we hypothesized to reflect tumour invasion capacity. After an additional 5 h (6 h post-PRISM injection), mice were scanned in a PET-CT imager for visualization of tumour number and size. As anticipated, 5-FU treatment in the CRC lung disease model significantly inhibited tumour progression compared with the non-treated cohort, which was apparent both in the decreased urinary reporter signal (Fig. 4a) and the PET imaging read-out (Fig. 4c), even after a single week of intervention. At the 2-week time point, untreated mice exhibited substantially increased tumour burden in the lung (Supplementary Fig. 14a,b) and disease had progressed to the point of requiring euthanasia. Quantitatively, the relative lung/liver ratio of the PET-CT signal in the cohort that received no treatment was over three times higher than that of the cohort treated with chemotherapy for 2 weeks (Fig. 4b,d). Consistent results were obtained when we applied the same longitudinal monitoring process to treated and untreated mice bearing CRC liver metastases (Fig. 4e–h and Supplementary Fig. 14c,d). This robust example of the dual-function single particle diagnostic PRISM nanosensor demonstrates the potential value of this tool when evaluating the efficacy of new candidate treatments, given the correspondence between the urinary sensor that reads out tumour invasion capacity and the acidosis-dependent imaging of the tumour itself. In other words, with the PRISM platform, we can monitor tumour size and activity in a single injection, which may help discriminate between therapeutic candidates that exhibit more or less effectiveness in both axes at the same time.

Discussion

We have developed a modular approach that leverages disease hallmarks to non-invasively detect cancer, localize malignant lesions for surgical intervention and longitudinally monitor drug response. In our approach, the remarkable concurrence of acidosis and MMPs across human cancer model systems was leveraged to achieve specific targeting of aggressive tumours. This non-invasive tool arose from the application of synthetic biomarkers to amplify

disease-associated protease activity and provide a concentrated urine-based read-out. The localization capability arose from acidosis-targeting and loading with ^{64}Cu enabling quantitative imaging by PET-CT. The multimodal monitoring of drug response arose from the longitudinal assessment of tumour nodules in both the lung and the liver by urinary reporter signals and PET-CT imaging in response to cytotoxic chemotherapy.

To minimize off-target effects, cancer diagnosis and therapy rely on active targeting strategies that are often limited to specific ligands expressed in diseases. Due to increased fermentative metabolism and poor perfusion, the extracellular pH in solid tumours is ubiquitously acidic (pH ≈ 6.5–6.9) compared with normal tissue under physiological conditions (pH ≈ 7.2–7.4)[19]. Such acidification is dynamic and heterogeneous as tumours progress, and the regions of highest tumour invasion correspond to the areas of lowest pH[27,31,38]. In our models, acidic regions marked by PRISM overlapped with the highly invasive regions at the tumour/stroma interface, where increased expression of MMPs was observed (Supplementary Figs. 3d and 12e). Engaging the aggressive population at the invasive front of tumours substantially improved the specificity of detection (Figs. 2 and 3). Although this work is not centred on the detection sensitivity of activity-based nanosensors, PRISM enables urinary signals to reveal tumours below 2 mm, informed by a pharmacokinetic mathematical model (Supplementary Figs. 15 and 16). Such prediction agreed with our previous report on tumour-penetrating ligand-functionalized activity-based nanosensors that enabled detection of nodules with median diameters smaller than 2 mm in an orthotopic model of human ovarian cancer[17]. To access the smallest tumour sizes that PRISM could detect, urinary tests performed shortly after initial transplantation of syngeneic CRC lung tumours showed differential urinary reporter signals just 7 days post-tumorigenesis, when the median histological diameters of disseminated tumour nodules were below 0.1 mm (Supplementary Fig. 17).

Optical, nuclear medicine and magnetic resonance imaging (MRI) probes allow visualization of acidic or proteolytic tumour microenvironments[14,39–41]. PET imaging using non-FDG radiotracers, such as nucleosides, amino acid analogues, antibodies and fragments, or polymers shows remarkable potential for tumour detection in organs with an undesirable metabolic background (that is, brain, heart and kidneys) or in low-FDG-uptake tumours[42–44]. Likewise, tumour-anchoring pHLIP-mediated PET-CT imaging overcame the insufficient tumour contrast through passive accumulation due to leaky tumour vasculature alone (Fig. 2f,g)[44], but also eliminated background signals in healthy surrounding tissue due to the high physiological uptake of FDG (Fig. 2d,e,h,i). PRISM allowed the detection of multiple cancer types through the ubiquitous presence of tumour acidosis (Supplementary Fig. 18), particularly in low-glucose-metabolizing colon tumours (Supplementary Fig. 13), shedding light on its use for diagnosing FDG-insensitive malignancies such as low-grade lung adenocarcinoma or mucinous neoplasms. Compared with PET imaging with radiolabelled pHLIP only, the polymerization of PRISM extended circulatory half-life and enhanced target recognition through multivalency (Supplementary Fig. 9b). Although PEGylation reduces accumulation in kidneys, the high uptake of pHLIP in naturally acidic regions (that is, renal cortical interstitium) may preclude the use of this agent for disease detection in these sites (that is, renal cell carcinoma)[45,46].

Despite its clinical utility in tumour diagnosis and staging, PET-CT with ^{18}F-FDG has a limited role in widespread primary cancer screening because of relatively low disease prevalence. Thus, conducting PET-CT in patients with positive molecular diagnostic results would improve its performance. We envision that the non-invasive, PRISM-based urine read-out could be applicable to at-risk patients, identified either due to risk factors or as requiring preventative monitoring following surgical tumour resection, offering an affordable and less time-intensive screening. When tumour occurrence is indicated by a longitudinal change in urinary signal, the quantitative signal derived from PET-CT imaging can be employed to confirm and localize tumour burden using the same core PRISM materials after loading them with a radiotracer on demand, thus eliminating unnecessary exposure to radioactivity. Therefore, beyond contributing to an initial diagnosis, PRISM can also be used in patient stratification leading to surgery with an intent to cure. This tool may also reveal regionally localized tumour responses, or non-responses, providing clinicians with even more robust and nuanced data with which to adjust treatment paradigms in a patient-specific manner. In the long run, we anticipate that pan-cancer tests will likely emerge that allow clinicians to assess patients for many cancers simultaneously at an annual check-up through a combination of molecular diagnostics. The principle of combining screening tests with on-demand diagnostic imaging may be incorporated into routine medical care, the feasibility of which has been encouraged in an exploratory trial on multicancer blood testing combined with PET-CT[3].

The PRISM platform represents a step towards establishing clinical actionability of molecular diagnostics in a single entity, but further in vivo validation is needed to confirm its generalizability beyond gastrointestinal cancers. The versatile sensor design enables detection of different extracellular hallmarks and the development of probes for variable imaging modalities such as near-infrared optical imaging, MRI or PET-MRI, depending on the disease location, anatomy and biology. Owing to the heterogeneity and benign disease aetiologies in human cancers, clinical trials will be necessary to accurately validate the clinical utility of such material, with the ultimate goal of improving the effectiveness of precision diagnostics.

Online content

Any methods, additional references, Nature Research reporting summaries, source data, extended data, supplementary information, acknowledgements, peer review information; details of author contributions and competing interests; and statements of data and code availability are available at https://doi.org/10.1038/s41563-021-01042-y.

Received: 6 October 2019; Accepted: 26 May 2021;
Published online: 15 July 2021

References

1. Punt, C. J., Koopman, M. & Vermeulen, L. From tumour heterogeneity to advances in precision treatment of colorectal cancer. *Nat. Rev. Clin. Oncol.* **14**, 235–246 (2017).
2. Siriwardena, A. K., Mason, J. M., Mullamitha, S., Hancock, H. C. & Jegatheeswaran, S. Management of colorectal cancer presenting with synchronous liver metastases. *Nat. Rev. Clin. Oncol.* **11**, 446–459 (2014).
3. Lennon, A. M. et al. Feasibility of blood testing combined with PET-CT to screen for cancer and guide intervention. *Science* **369**, eabb9601 (2020).
4. Bach, P. B. et al. Benefits and harms of CT screening for lung cancer: a systematic review. *JAMA* **307**, 2418–2429 (2012).
5. Chabon, J. J. et al. Integrating genomic features for non-invasive early lung cancer detection. *Nature* **580**, 245–251 (2020).
6. Cohen, J. D. et al. Detection and localization of surgically resectable cancers with a multi-analyte blood test. *Science* **359**, 926–930 (2018).
7. Liu, M. C. et al. Sensitive and specific multi-cancer detection and localization using methylation signatures in cell-free DNA. *Ann. Oncol.* **31**, 745–759 (2020).
8. Aalipour, A. et al. Engineered immune cells as highly sensitive cancer diagnostics. *Nat. Biotechnol.* **37**, 531–539 (2019).
9. Kirkpatrick, J. D. et al. Urinary detection of lung cancer in mice via noninvasive pulmonary protease profiling. *Sci. Transl. Med.* **12**, eaaw0262 (2020).
10. Rakhit, C. P. et al. Early detection of pre-malignant lesions in a KRAS(G12D)-driven mouse lung cancer model by monitoring circulating free DNA. *Dis. Model Mech.* **12**, dmm036863 (2019).
11. Hori, S. S. & Gambhir, S. S. Mathematical model identifies blood biomarker-based early cancer detection strategies and limitations. *Sci. Transl. Med.* **3**, 109ra116 (2011).

12. van der Stok, E. P., Spaander, M. C. W., Grunhagen, D. J., Verhoef, C. & Kuipers, E. J. Surveillance after curative treatment for colorectal cancer. *Nat. Rev. Clin. Oncol.* **14**, 297–315 (2017).
13. Rojas Llimpe, F. L. et al. Imaging in resectable colorectal liver metastasis patients with or without preoperative chemotherapy: results of the PROMETEO-01 study. *Br. J. Cancer* **111**, 667–673 (2014).
14. Weissleder, R., Tung, C. H., Mahmood, U. & Bogdanov, A. Jr In vivo imaging of tumors with protease-activated near-infrared fluorescent probes. *Nat. Biotechnol.* **17**, 375–378 (1999).
15. Ronald, J. A., Chuang, H. Y., Dragulescu-Andrasi, A., Hori, S. S. & Gambhir, S. S. Detecting cancers through tumor-activatable minicircles that lead to a detectable blood biomarker. *Proc. Natl Acad. Sci. USA* **112**, 3068–3073 (2015).
16. Kwong, G. A. et al. Mass-encoded synthetic biomarkers for multiplexed urinary monitoring of disease. *Nat. Biotechnol.* **31**, 63–70 (2013).
17. Kwon, E. J., Dudani, J. S. & Bhatia, S. N. Ultrasensitive tumour-penetrating nanosensors of protease activity. *Nat. Biomed. Eng.* **1**, 0054 (2017).
18. Dudani, J. S., Ibrahim, M., Kirkpatrick, J., Warren, A. D. & Bhatia, S. N. Classification of prostate cancer using a protease activity nanosensor library. *Proc. Natl Acad. Sci. USA* **115**, 8954–8959 (2018).
19. Webb, B. A., Chimenti, M., Jacobson, M. P. & Barber, D. L. Dysregulated pH: a perfect storm for cancer progression. *Nat. Rev. Cancer* **11**, 671–677 (2011).
20. Quail, D. F. & Joyce, J. A. Microenvironmental regulation of tumor progression and metastasis. *Nat. Med.* **19**, 1423–1437 (2013).
21. Hanahan, D. & Weinberg, R. A. Hallmarks of cancer: the next generation. *Cell* **144**, 646–674 (2011).
22. Cremolini, C. et al. First-line chemotherapy for mCRC—a review and evidence-based algorithm. *Nat. Rev. Clin. Oncol.* **12**, 607–619 (2015).
23. Weerakkody, D. et al. Family of pH (low) insertion peptides for tumor targeting. *Proc. Natl Acad. Sci. USA* **110**, 5834–5839 (2013).
24. Wyatt, L. C. et al. Peptides of pHLIP family for targeted intracellular and extracellular delivery of cargo molecules to tumors. *Proc. Natl Acad. Sci. USA* **115**, E2811–E2818 (2018).
25. Danino, T. et al. Programmable probiotics for detection of cancer in urine. *Sci. Transl. Med.* **7**, 289ra284 (2015).
26. Dumitru, C. D., Antonysamy, M. A., Tomai, M. A. & Lipson, K. E. Potentiation of the anti-tumor effects of imidazoquinoline immune response modifiers by cyclophosphamide. *Cancer Biol. Ther.* **10**, 155–165 (2010).
27. Estrella, V. et al. Acidity generated by the tumor microenvironment drives local invasion. *Cancer Res.* **73**, 1524–1535 (2013).
28. Corbet, C. & Feron, O. Tumour acidosis: from the passenger to the driver's seat. *Nat. Rev. Cancer* **17**, 577–593 (2017).
29. Kalbasi, A. & Ribas, A. Tumour-intrinsic resistance to immune checkpoint blockade. *Nat. Rev. Immunol.* **20**, 25–39 (2019).
30. Holohan, C., Van Schaeybroeck, S., Longley, D. B. & Johnston, P. G. Cancer drug resistance: an evolving paradigm. *Nat. Rev. Cancer* **13**, 714–726 (2013).
31. Rohani, N. et al. Acidification of tumor at stromal boundaries drives transcriptome alterations associated with aggressive phenotypes. *Cancer Res.* **79**, 1952–1966 (2019).
32. Damaghi, M. et al. Chronic acidosis in the tumour microenvironment selects for overexpression of LAMP2 in the plasma membrane. *Nat. Commun.* **6**, 8752 (2015).
33. Swietach, P., Vaughan-Jones, R. D. & Harris, A. L. Regulation of tumor pH and the role of carbonic anhydrase 9. *Cancer Metastasis Rev.* **26**, 299–310 (2007).
34. Kumar, S. et al. Magnetic resonance imaging in lung: a review of its potential for radiotherapy. *Br. J. Radiol.* **89**, 20150431 (2016).
35. Longo, D. L. et al. In vivo imaging of tumor metabolism and acidosis by combining PET and MRI-CEST pH imaging. *Cancer Res.* **76**, 6463–6470 (2016).
36. Roper, J. et al. Corrigendum: in vivo genome editing and organoid transplantation models of colorectal cancer and metastasis. *Nat. Biotechnol.* **35**, 1211 (2017).
37. Walker-Samuel, S. et al. In vivo imaging of glucose uptake and metabolism in tumors. *Nat. Med.* **19**, 1067–1072 (2013).
38. Chiche, J. et al. Hypoxia-inducible carbonic anhydrase IX and XII promote tumor cell growth by counteracting acidosis through the regulation of the intracellular pH. *Cancer Res.* **69**, 358–368 (2009).
39. Yuan, Y. et al. Furin-mediated intracellular self-assembly of olsalazine nanoparticles for enhanced magnetic resonance imaging and tumour therapy. *Nat. Mater.* **18**, 1376–1383 (2019).
40. Lindeman, L. R. et al. Differentiating lung cancer and infection based on measurements of extracellular pH with acidoCEST MRI. *Sci. Rep.* **9**, 13002 (2019).
41. Park, J. H. et al. Magnetic iron oxide nanoworms for tumor targeting and imaging. *Adv. Mater.* **20**, 1630–1635 (2008).
42. Jailkhani, N. et al. Noninvasive imaging of tumor progression, metastasis, and fibrosis using a nanobody targeting the extracellular matrix. *Proc. Natl Acad. Sci. USA* **116**, 14181–14190 (2019).
43. Larimer, B. M. et al. Granzyme B PET imaging as a predictive biomarker of immunotherapy response. *Cancer Res.* **77**, 2318–2327 (2017).
44. Huang, G. et al. PET imaging of occult tumours by temporal integration of tumour-acidosis signals from pH-sensitive ^{64}Cu-labelled polymers. *Nat. Biomed. Eng.* **4**, 314–324 (2020).
45. Wyatt, L. C., Lewis, J. S., Andreev, O. A., Reshetnyak, Y. K. & Engelman, D. M. Applications of pHLIP technology for cancer imaging and therapy. *Trends Biotechnol.* **35**, 653–664 (2017).
46. Viola-Villegas, N. T. et al. Understanding the pharmacological properties of a metabolic PET tracer in prostate cancer. *Proc. Natl Acad. Sci. USA* **111**, 7254–7259 (2014).

Methods

Peptide and peptide conjugate synthesis and characterization. Information on all the peptides used in this study is listed in Supplementary Table 1. Peptides were synthesized by CPC Scientific unless otherwise indicated. All commercially synthesized peptides were purified by the vendor using reversed-phase HPLC on a Phenomenex Luna C18 column to >90% purity. The molecular masses of purified peptides were verified by mass spectrometric analysis. A variant of pHLIP (pHLIP-V3) with improved imaging capacity was used in the study[23]; the peptide was stabilized with two lysine residues at the C terminus to improve its solubility and purity in solid-phase synthesis. Peptide conjugates were prepared by covalently conjugating maleimide-containing fluorophores or the metal chelator NOTA (Macrocyclics, B-622) to the single cysteine residue of the peptide. To label pHLIP-V3, the peptide was dissolved in *N*,*N*-dimethylformamide/H_2O (1:4; Sigma-Aldrich) at 2 mg ml^{-1}, followed by the slow addition of 5 equiv. of maleimide-containing fluorophore or chelator in an equal volume of phosphate buffer (0.1 M, pH 7.0). The reaction was conducted at room temperature for at least 4 h. Similarly, the non-targeting control peptide was dissolved at 1 mg ml^{-1} in H_2O and allowed to react with 5 equiv. of fluorophore or chelator at room temperature for at least 4 h. The resulting peptide conjugates were washed three times using Amicon centrifugal filter units (molecular weight cut-off (MWCO) 3 kDa, MilliporeSigma) and analysed on an Agilent Model 1100 HPLC system with a Vydac 214TP510 C4 column using ChemStation software. The HPLC gradient was set to start from 5% A buffer (0.05% TFA in H2O), kept isocratic for 20 min, and reached 80% B buffer (0.05% TFA, 99.95% acetonitrile) at 65 min with a flow rate of 0.3 ml min^{-1}. Purified conjugates were validated by matrix-assisted laser desorption/ionization–time of flight (MALDI–TOF) mass spectrometry (Microflex MALDI–TOF, Bruker) using α-cyano-4-hydroxycinnamic acid as matrix. To screen for MMP9 with optimal signal-to-background ratio, intramolecular-quenched peptides were used in fluorometric protease cleavage assays. The peptide substrate sequence selected was tagged with the D stereoisomer of glutamate fibrinopeptide, flanked by biotin and FAM ligands as the urinary reporter for in vivo experiments.

Nanosensor synthesis and characterization. Multivalent PEG with reactive groups (40 kDa, eight-arm, JenKem Technology) was dissolved in Chelex 100 resin (Bio-Rad Laboratories)-processed phosphate buffer (0.1 M, pH 7.0) and filtered (pore size 0.2 µm). After filtration, an equimolar mixture of azide-containing pHLIP-V3 (or the non-targeting control peptide or peptides conjugated with fluorophore or chelator) and urinary reporter peptides was added at twofold molar excess with respect to the DBCO groups on the eight-arm PEG (pHLIP-V3 or NT-V3/reporter/DBCO = 1:1:1) and allowed to react for at least 4 h at room temperature. The nanosensors were washed three times using Amicon centrifugal filter units (MWCO 10 kDa, MilliporeSigma) to separate them from unconjugated peptides, and further purified using fast protein liquid chromatography (ÄKTA purifier 10, GE Healthcare) with a Superdex 75 10/300GL column. Concentrations were quantified from the extinction coefficients of the ligands. The nanosensors were stored at 4 °C in PBS. Dynamic light scattering (Zeta Sizer Nanoseries, Malvern Instruments) was used to characterize the hydrodynamic diameter of the nanosensors. The ratio of pHLIP-V3 or the non-targeting control peptide and the MMP substrate on the sensors was quantified by measuring the absorbance of Cy7-labelled pHLIP-V3-F or NT-V3-F (750 nm) and FAM-labelled MMP9 substrate (495 nm) by UV–Vis spectroscopy using a Nanodrop spectrophotometer (Thermo Scientific).

Transcriptomic analysis. RNA-Seq data of two carcinomas (BRCA, COAD) and one blastoma (GBM) were obtained from The Cancer Genome Atlas (TCGA) Research Network (http://cancergenome.nih.gov). Differential gene expression was analysed at the BioMicro Center at MIT using transcriptomic data from both tumour and control samples. The BRCA datasets contain 1,093 tumour samples and 112 normal tissue samples, the COAD datasets involve 285 tumour samples and 41 normal tissue samples, and the GBM datasets include 153 tumour samples and 5 normal tissues samples. Briefly, next-generation sequencing reads were mapped to the mouse mm10 reference genome using STAR/2.5.3a. Gene expression calculations were performed using RSEM/1.3.0. Differential expression analyses were carried out using DESeq2 1.10.1. The expression profiles of particular genes of interest among multiple tumour types were downloaded from FireBrowse (http://firebrowse.org).

Circular dichroism. Acidosis-targeting peptide (V3) and its non-targeting counterpart were dissolved at 1 mg ml^{-1} in 20 mM HEPES buffer (pH 7.4) or 20 mM MES (pH 6.0), respectively. Circular dichroism spectra were recorded at 0.2 mg ml^{-1} at 25 °C on a JASCO J-1500 model circular dichroism spectrometer. The molar ellipticity was determined on the basis of the CD signal and peptide sample concentration.

Cryogenic transmission electron microscopy. In sample preparation for cryo-electron microscopy, 3 µl of sensors at 0.5-1 mg/mL (concentration was quantified by absorbance of FAM on MMP responsive peptide) in PBS was dropped on a lacey copper grid coated with a continuous carbon film and blotted to remove excess sample without damaging the carbon layer by Gatan Cryo Plunge III. The grid was mounted on a Gatan 626 single-tilt cryo-holder in the TEM column. The specimen and holder tip were cooled using liquid nitrogen, which was maintained during the transfer into the microscope and subsequent imaging. Imaging on a JEOL 2100 FEG microscope was performed using the minimum dose method, which was essential to avoid sample damage under the electron beam. The microscope was operated at 200 kV with magnification in the range of 10,000–60,000 to assess particle size and distribution. All images were recorded on a Gatan 2K × 2K UltraScan CCD camera.

Cell culture and flow cytometry. Mouse cell lines MC26-LucF (carrying firefly luciferase, from the Kenneth K. Tanabe Laboratory, Massachusetts General Hospital), D8-175 KPC-derived pancreatic cancer line (from the Tyler Jacks Laboratory, Massachusetts Institute of Technology) and 4T1 (ATCC CRL-2539), and human cell lines MDA-MB-435 (NCI-60) and U937 (ATCC CRL-1593.2) were cultured in DMEM (Gibco) medium supplemented with 10% (v/v) fetal bovine serum (FBS; Gibco) and 1% (v/v) penicillin–streptomycin (CellGro) at 37 °C and in 5% CO_2. OVCAR8 (NCI-60) and LS 174T (ATCC CL-188) cell lines were grown in RPMI1640 (Gibco) or EMEM (Gibco) medium supplemented with 10% (v/v) FBS and 1% (v/v) penicillin–streptomycin, respectively. All cell lines tested negative for mycoplasma contamination. To alter the pH conditions in the medium for each cell line, the sodium bicarbonate concentration was adjusted in the base medium according to the Henderson–Hasselbalch equation to reach the target pH. Media were equilibrated at 37 °C and in 5% CO_2 for at least 12 h prior to use. For flow cytometry analyses, cells cultured in six-well plates were treated with 10 µM of fluorescent-labelled pHLIP nanosensors at physiological (7.4) or acidic pH (6.4). Cells were collected by pipetting with and resuspending in DAPI (0.5 µg ml^{-1})-containing PBS (pH 7.4 or 6.4) and analysed on a BD LSRII flow cytometer immediately. Data were analysed in FlowJo (TreeStar Software).

Animal models. All animal studies were approved by the Massachusetts Institute of Technology Committee on Animal Care (MIT protocol 0417-025-20 and 0217-014-20). Animals were maintained in the Koch Cancer Institute animal facility with a 12-h light/12-h dark cycle at ~18–23 °C and ~50% humidity. All animals received humane care, and all experiments were conducted in compliance with institutional and national guidelines and supervised by staff from the Division of Comparative Medicine of the Massachusetts Institute of Technology. The CRC lung metastasis model was generated by intravenous injection of 1×10^5 luciferized mouse MC26 cells into female BALB/c mice (6–8 weeks, Taconic). To generate a liver metastasis model of CRC, immunocompetent 6–8-week-old female BALB/c mice (Taconic) were injected with 5×10^4 luciferized MC26 cells in the subsplenic capsule to allow cells to seed the liver. After 90 s, the spleen was removed to prevent splenic tumours. Four-to-five-week-old female NCr nude mice (Taconic) were injected bilaterally with 2×10^6 LS 174T cells per flank to generate subcutaneous xenografts, or implanted with 5×10^5 D8-175 KPC cells to form flank pancreatic cancer allografts. Syngeneic subcutaneous grafts were generated by inoculation of 1×10^5 MC26 cells in BALB/c mice. Tumour growth was monitored by luminescence using the In Vivo Imaging System (IVIS, PerkinElmer). Prior to the induction of tumours, urine measurements were performed by injecting nanosensors at 1 nmol (peptide substrate amount) per mouse. Post-tumour inoculation urine measurements were performed when tumour luminescence reached an average of $(1-1.5) \times 10^7$ photons s^{-1} cm^{-2} sr^{-1}. After injection with nanosensors, mice were placed into custom housing with a 96-well plate base for urine collection. Their bladders were voided to collect between 100–200 µl urine 1 and 2 h post-injection. The urine was centrifuged and stored at −20 °C. For organ and tumour biodistribution and quantification, mice were sacrificed 6 or 24 h post-nanosensor injection, and organs were removed and scanned using the LI-COR Odyssey Infrared Imaging System with ImageStudio (PerkinElmer). Fluorescence from the peptides on nanoparticle scaffolds was quantified using ImageJ software. To examine the toxicity, 2 nmol nanosensors (peptide substrate amount) were injected intravenously. After scarification, the organs were fixed, paraffin-embedded, sectioned and stained with haematoxylin and eosin.

Mouse treatments. 5-FU was purchased (Sigma-Aldrich) and prepared as previously described[47]. 5-FU or a vehicle control (DMSO) was administered to mice by intraperitoneal injection, in a volume of 0.2 ml, 1 week after cell injection for metastasis-initiation experiments. A dose of 15 mg per kg per treatment was used in all experiments. Tumour-bearing mice were treated daily for 4 days, followed by once every other day until the end of the study. Experimental group sizes were determined by the number of mice housed per cage ($n = 5$ mice per cage). For treatment experiments, tumour inoculation cohorts were designed to have $n = 10$ mice per group (one more cage as needed), from which $n = 5$ animals were chosen to perform studies on to balance a similar range of tumour burden between the groups based on tumour signals quantified by IVIS. Tumour-bearing mice were closely monitored and euthanized following health-check advice given by an independent veterinary scientist responsible for animal welfare.

Urine reporter analysis and in vitro protease activity assays. The urinary reporter tagged with a biotin-FAM ligand pair was quantified using custom

sandwich ELISA assays that have been previously described[48]. The ligand pair was recognized by a mouse anti-fluorescein antibody (GeneTex, GTX10257) and NeutrAvidin–horseradish peroxidase (HRP; Pierce). Protease activity assays were performed in a 384-well plate in duplicate in MMP-specific buffer (50 mM Tris, pH 7.5, 10 mM $CaCl_2$, 300 mM NaCl, 20 μM $ZnCl_2$, 0.02% Brij-35 and 1% BSA) with intramolecular-quenched peptides (1 μM) and recombinant proteases (12.5 nM) in 30 μl at 37 °C. All recombinant enzymes were purchased from Enzo Life Sciences. Fluorescence was measured at excitation/emission wavelengths of 485/535 nm using an Infinite 200 PRO Tecan plate reader with Tecan iControl software. Tissue samples were homogenized in cold PBS and centrifuged before total protein quantification using the Pierce BCA Protein Assay Kit (Thermo Fisher). Supernatant (5 μl, 1 mg ml^{-1} total protein) was added to the 384-well plate with 25 μl FRET peptides (1 μM) in MMP-specific buffer. Marimastat (Sigma) was used at a final concentration of 50 μM.

Radiolabelling of PRISM, PET-CT imaging and analysis. ^{64}Cu in the form of aqueous copper chloride liquid was obtained from the Mallinckrodt Institute of Radiology Cyclotron Facility, Washington University School of Medicine in St. Louis. The ^{64}Cu stock solution was equilibrated in 1× PBS solution prior to adding to maleimide-NOTA-labelled PRISM or non-targeting sensors in 1× PBS. The labelling reaction was allowed to proceed at room temperature for 20 min and then loaded on an Amicon Ultra centrifugal filter (MWCO 10 kD, MilliporeSigma). Free ^{64}Cu was separated by two 10-min spins at 12,000*g*, the remaining activity in the nanosensors was measured using a CRC-25R dose calibrator (Mirion Technologies) and the ^{64}Cu-chelated nanosensors were adjusted to ~100 μCi in 200 μl saline per mouse for intravenous injection.

Animal PET-CT imaging was performed on a G8 PET-CT preclinical imaging system (PerkinElmer) with a G8 Acquisition Engine. In all experiments involving direct comparison of ^{18}F-FDG and ^{64}Cu-PRISM, animals were first imaged with ^{18}F-FDG, followed by subsequent ^{64}Cu-PRISM imaging 2 days later according to the availability of radioactive traces. Mice were fasted for 12 h prior to PET-CT imaging with ^{18}F-FDG. Each animal was anaesthetized with isoflurane (2.5% for induction, 1.5–2% for maintenance in a heated chamber for ^{18}F-FDG scanning). After placement of a catheter in the lateral tail vein for probe administration, mice were positioned in the imaging shuttle and a bolus injection (mean ~120 μCi) was delivered. Static imaging was performed for 10 min (1 frame) for sham and tumour-bearing mice 1 h post-injection of ^{18}F-FDG or 6 h post-injection of ^{64}Cu-PRISM. Whole-body CT was performed immediately after the PET acquisition. CT images were acquired over ~1 min (peak tube voltage, 50 kV; tube current, 200 μA). The PET data were reconstructed using a three-dimensional maximum-likelihood expectation–maximization algorithm run over 60 iterations. Normalization, decay-correction, attenuation-correction and dead time-correction were applied to all PET data acquired in listmode. Reconstructed PET and CT data were quantitatively evaluated using VivoQuant software (inviCRO). Regions of interest (ROIs) were drawn on the CT images in all planes (coronal, sagittal and transverse). The radioactivity uptake values within CT-imaged organs were obtained from mean voxel values within the ROI and converted into percentage injected dose (%ID) and then divided by mouse mass (g) to obtain an imaging ROI-derived percentage of the injected radioactive dose per gram of tissue (%ID g^{-1}). The size of the ROI was ~465 mm^3 for the lungs and ~503 mm^3 for the liver. Tumour (or tissue)-to-tissue (that, is lung-to-liver) ratios were calculated by dividing the mean lung by the mean liver %ID g^{-1} values. To quantify the radioactivity in diseased tissues ex vivo, tissues were collected after perfusion with PBS and counts were collected using a 2480 WIZARD2 gamma counter (Perkin Elmer). A small fraction of the prepared dose was run as a count standard along with the tissues to quantify the percentage injected dose per sample. All samples were decay-corrected to the count standard measurement time.

Cryo-fluorescence tomography. CFT is a molecular tissue imaging modality developed by EMIT imaging. Immediately following PET imaging, the mice were sacrificed and the whole animals were frozen by slowly submerging the animals in dry ice-cooled hexanes. The animals were left in hexanes for 5–10 min to allow them to freeze completely and then treated with optimum cutting temperature (OCT) compound. Tissue sectioning and imaging were performed on an EMIT Xerra platform. To visualize the FAM fluorophore in PRISM, excitation was set at 470 nm with emission at 511/20 nm. A deck of 25-μm tissue slices were imaged by a VivID Multi resolution viewer and reconstructed using VivoQuant software (inviCRO).

Histology and immunohistochemistry. Sectioning and staining were performed at the KI Histology Core. Organs were fixed in 4% paraformaldehyde (PFA) and stored at 4 °C prior to embedding in paraffin, sectioning and staining. Slides were stained with primary antibodies in accordance with manufacturer instructions, followed by HRP secondary antibodies, and were digitized using a 3DHistech P250 high capacity slide scanner (Perkin Elmer). Image visualization and analysis were conducted with CaseViewer software (3DHISTECH). Multiple organ cancer and normal tissue microarrays were obtained from US Biomax (catalogue number CO702b). The TMA slides were stained with anti-MMP9 antibody (Abcam ab38898; 1:500) and anti-CAIX antibody (Abcam ab15086, 1:200). Blind expression scoring of cores was performed by R. T. Bronson at the KI Histology Core.

Confocal microscopy and immunofluorescence. Cells were seeded in a Nunc Lab-Tek Chambered Coverglass system (Thermo Fisher) in physiological (7.4) or acidic pH (6.4), incubated with VivoTag645-labelled pHLIP nanosensors and imaged under a Zeiss LSM 700 inverted confocal scanning microscope with an excitation wavelength of 633 nm and emission filter of 660–710 nm. Acquired images were processed with ZEN software (Carl Zeiss Microscopy). To track the localization of nanosensors in vivo, tumour tissues were extracted, briefly fixed in 2% PFA, placed in 30% sucrose overnight and embedded in OCT compound prior to sectioning. The OCT-embedded tissue sections were stained with anti-FITC antibody (GeneTex GTX19224, 1:1,000), anti-MMP9 antibody (Abcam ab38898; 1:500) or anti-biotin antibody (Abcam ab201341, 1:200). Fluorescence-labelled secondary antibodies (Invitrogen, 1 μg ml^{-1}) were applied according to the primaries for 30 min at room temperature. The colocalization of MMP9 immunofluorescence and PRISM-labelled acidic areas in tumour sections was analysed using ImageJ and quantified for the percentage of overlap between markers in the red and green channels using inForm software (Perkin Elmer). Image quantification included tissue segmentation to segment tumour and non-tumour regions, followed by cell segmentation by DAPI counterstain using built-in algorithms. The numbers of MMP9-positive and PRISM-positive cells were quantified in at least three areas per tumour section from at least three animals. The MMP9-positive and PRISM-positive cells were quantified by cell-based overlap and Pearson correlation coefficient analyses. The average percentages of negative, single and double positive cells in each channel were reported.

Statistics and reproducibility. Statistical analyses were conducted in GraphPad Prism. Data are presented as the mean with standard deviation (s.d.) or standard error of the mean (s.e.m.). To determine whether there were any statistically significant differences between the means of independent groups, the two-tailed *t*-test was used for two groups of data (parametric), and ANOVA was used for multiple group comparisons. Details of sample sizes, statistical tests and reproducibility of experiments are specified in the figure legends.

Reporting Summary. Further information on research design is available in the Nature Research Reporting Summary linked to this article.

Data availability

The Cancer Genome Atlas (TCGA) Research Network (http://cancergenome.nih.gov) and FireBrowse (http://firebrowse.org) are open access resources with enriched cancer genomics data. All data that support the findings of this study are available within the article and Supplementary Information or from the corresponding author (sbhatia@mit.edu) upon reasonable request.

Code availability

The accompanying code can be found on GitHub (https://github.com/lhaomit/PK-model-for-PRISM). The code was run on MATLAB_R2018b. The model description is available in the Supplementary Information.

References

47. Chang, J. et al. Chemotherapy-generated cell debris stimulates colon carcinoma tumor growth via osteopontin. *FASEB J.* **33**, 114–125 (2019).
48. Warren, A. D., Kwong, G. A., Wood, D. K., Lin, K. Y. & Bhatia, S. N. Point-of-care diagnostics for noncommunicable diseases using synthetic urinary biomarkers and paper microfluidics. *Proc. Natl Acad. Sci. USA* **111**, 3671–3676 (2014).
49. Bhatia, S. N. et al. Sensors for detecting and imaging of cancer metastasis. US Patent Application No. 16/745,748 (2020).

Acknowledgements

We thank the Koch Institute Swanson Biotechnology Center for technical support, specifically V. Spanoudaki, S. Malstrom, M. Pandya and S. Elmiligy from the KI Animal Imaging & Preclinical Testing Core for assistance with PET-CT and IVIS imaging; M. Farhoud and P. Zakrzewski from Emit Imaging for cryo-fluorescence tomography; K. Cormier from the KI Histology Core for tissue sectioning and staining; D. Yun from the KI Nanotechnology Materials Core for electron microscopy imaging; R. Cook and A. Leshinsky from the KI Biopolymers & Proteomics Core for HPLC and mass spectrometry; W. Salman from the Keck Microscopy Facility for confocal microscopy; and D. Ma from the KI Bioinformatics & Computing Core for assistance with transcriptome data analysis. We also thank A. Warren for initial discussions of this work; A. Soleimany and J. Voog for critical reading of the manuscript. This study was supported in part by a Koch Institute Support Grant (P30-CA14051) from the National Cancer Institute (Swanson Biotechnology Center), a Core Center Grant (P30-ES002109) from the National Institute of Environmental Health Sciences, by the Koch Institute Frontier Research Program via the Casey and Family Foundation Cancer Research

Fund, the Virginia and D.K. Ludwig Fund for Cancer Research, and the Koch Institute Marble Center for Cancer Nanomedicine. L.H. was supported by a KI Quinquennial Cancer Research Fellowship and fellowships from the American Cancer Society and the Ludwig Center for Molecular Oncology at MIT. S.N.B is a Howard Hughes Medical Institute investigator. This study is dedicated to Sanjiv Sam Gambhir, who inspired a generation of scientists with his vision for the role of precision health and integrated diagnostics and whom we tragically lost too soon.

Author contributions

L.H., H.E.F., F.B.G. and S.N.B. conceived and designed the research. L.H. carried out all the experiments and analysed the data. N.R. performed the immunofluorescent studies and data analysis. R.T.Z., E.M.P. and H.K. assisted with the animal studies. H.M. assisted with the PET-CT imaging. O.J.K. assisted with the PET-CT data analysis. L.H., H.E.F. and S.N.B. wrote the manuscript with feedback from all the authors.

Competing interests

S.N.B. and L.H. are listed as inventors on a patent application[49] related to the content of this work. S.N.B. holds equity in Glympse Bio, Satellite Bio, Cend Therapeutics and Catalio Capital; is a director at Vertex; consults for Moderna, and receives sponsored research funding from Johnson & Johnson. All the other authors declare no competing interests.

Additional information

Supplementary information The online version contains supplementary material available at https://doi.org/10.1038/s41563-021-01042-y.

Correspondence and requests for materials should be addressed to S.N.B.

Peer review information *Nature Materials* thanks Jeff Bulte and the other, anonymous, reviewer(s) for their contribution to the peer review of this work.

Reprints and permissions information is available at www.nature.com/reprints.

nature research

Corresponding author(s): Sangeeta N. Bhatia

Last updated by author(s): Apr 16, 2021

Reporting Summary

Nature Research wishes to improve the reproducibility of the work that we publish. This form provides structure for consistency and transparency in reporting. For further information on Nature Research policies, see our Editorial Policies and the Editorial Policy Checklist.

Statistics

For all statistical analyses, confirm that the following items are present in the figure legend, table legend, main text, or Methods section.

n/a	Confirmed	
☐	☒	The exact sample size (*n*) for each experimental group/condition, given as a discrete number and unit of measurement
☐	☒	A statement on whether measurements were taken from distinct samples or whether the same sample was measured repeatedly
☐	☒	The statistical test(s) used AND whether they are one- or two-sided *Only common tests should be described solely by name; describe more complex techniques in the Methods section.*
☐	☒	A description of all covariates tested
☐	☒	A description of any assumptions or corrections, such as tests of normality and adjustment for multiple comparisons
☐	☒	A full description of the statistical parameters including central tendency (e.g. means) or other basic estimates (e.g. regression coefficient) AND variation (e.g. standard deviation) or associated estimates of uncertainty (e.g. confidence intervals)
☐	☒	For null hypothesis testing, the test statistic (e.g. *F*, *t*, *r*) with confidence intervals, effect sizes, degrees of freedom and *P* value noted *Give P values as exact values whenever suitable.*
☒	☐	For Bayesian analysis, information on the choice of priors and Markov chain Monte Carlo settings
☒	☐	For hierarchical and complex designs, identification of the appropriate level for tests and full reporting of outcomes
☐	☒	Estimates of effect sizes (e.g. Cohen's *d*, Pearson's *r*), indicating how they were calculated

Our web collection on statistics for biologists contains articles on many of the points above.

Software and code

Policy information about availability of computer code

Data collection	G8 Acquisition Engine (Version 2.1.1.0) was used to collect data on G8 PET/CT preclinical imaging system (PerkinElmer Inc.). Tecan icontrol software (Version 3.7.3.0) was used to collect data on Tecan Infinite 200pro microplate reader (Tecan Group Ltd.). ImageStudio (Version 5.2, Li-Cor Inc.) was used to collect data on Odyssey CLx imaging system (Li-Cor Inc.). Living Image (Version 4.5.5, PerkinElmer Inc.) was used to collect data on IVIS spectrum optical imaging system (PerkinElmer Inc.). Panoramic Scanner (Version 1.22) was used to collect data on 3D Histech P250 High Capacity Slide Scanner (PerkinElmer Inc.). ChemStation for LC 3D (Rev. B.03.01, Agilent Technologies Inc.) was used to control the Agilent Model 1100 HPLC system. The code of the pharmacokinetic model was run on MATLAB_R2018b. Details are specified in Methods, Figure Legends and Supplementary Information.
Data analysis	VivoQuant software (Version 4.0 patch3, InviCRO Inc.) was used for PET/CT image analysis. ZEN Software (Carl Zeiss, Jena, Germany) was used for confocal microscopy image analysis. ImageStudio (Version 5.2, Li-Cor Inc.) was used for near-infrared image analysis. Living Image (Version 4.7.3, Perkin Elmer Inc.) was used for IVIS in vivo optical imaging analysis. CaseViewer (Version 2.2, 3DHISTECH Ltd.) was used for visualization of images collected on the 3D Histech P250 High Capacity Slide Scanner. Zen software (Version 2.2.58, Carl Zeiss Microscopy, LLC.), ImageJ (1.48v, NIH) and inForm software (Version 2.3, PerkinElmer Inc.) were used for all other image analyses. FlowJo (TreeStar Software Version 9.9.6) was used for Flow Cytometry data analysis. Differential expression analyses were carried out by DESeq2 1.10.1. GraphPad Prism (Version 9) was used for data analysis and statistics. Details are specified in Methods, Figure Legends and Supplementary Information.

For manuscripts utilizing custom algorithms or software that are central to the research but not yet described in published literature, software must be made available to editors and reviewers. We strongly encourage code deposition in a community repository (e.g. GitHub). See the Nature Research guidelines for submitting code & software for further information.

Data

Policy information about availability of data

All manuscripts must include a data availability statement. This statement should provide the following information, where applicable:

- Accession codes, unique identifiers, or web links for publicly available datasets
- A list of figures that have associated raw data
- A description of any restrictions on data availability

The Cancer Genome Atlas (TCGA) Research Network (http://cancergenome.nih.gov) and FireBrowse (http://firebrowse.org) are open access resources with enriched cancer genomics data. All data that support the findings of this study are available within the article and Supplementary Information or from the corresponding author (sbhatia@mit.edu) upon reasonable request.

Field-specific reporting

Please select the one below that is the best fit for your research. If you are not sure, read the appropriate sections before making your selection.

☒ Life sciences ☐ Behavioural & social sciences ☐ Ecological, evolutionary & environmental sciences

For a reference copy of the document with all sections, see nature.com/documents/nr-reporting-summary-flat.pdf

Life sciences study design

All studies must disclose on these points even when the disclosure is negative.

Sample size	Sample size is indicated in the figure legend for each experiment whenever possible. No sample-size calculations were performed. Sample size was determined to be adequate based on the magnitude and consistency of measurable differences between groups. Samples were allowed to have at least three biological replicates to derive statistical significance. For animal studies, experimental group sizes were practically associated according to the number of mice housed per cage (n=5 mice per cage).
Data exclusions	No data was excluded for in vitro experiments. Pre-established exclusion criteria were set based on failed injection or urine production within defined time course of the animal study. Animals were excluded solely on the basis of the pre-established exclusion criteria.
Replication	All experiments were repeated independently with similar results. In vitro and in vivo investigation of nanosensors were typically performed for three times, except for the human tissue microarray analysis, in vivo treatment monitoring experiments were completed twice independently. For immunofluorescence staining, tissue sections were independently stained by three investigators.
Randomization	In vitro samples were prepared, processed and analyzed in a random order. Grouping criteria of animals was included in methods and figure legends. All animals analyzed in this study were sex- and age-matched. For drug treatment experiments, animals were chosen to balance a similar range of tumor burden between the groups based on tumor signals quantified by IVIS to perform studies on. Animals receiving PRISM or control sensor were randomly selected.
Blinding	For immunohistochemistry analysis of human tissue microarrays, specimens were analyzed by a veterinary pathologist who was blinded to the treatment groups. In all other cases, investigators were not blinded to the groups and treatments during experiments, because the investigators who set up the experiments carried out the analyses. Data reported for these experiments are not subjective but based on the quantitative assays described.

Reporting for specific materials, systems and methods

We require information from authors about some types of materials, experimental systems and methods used in many studies. Here, indicate whether each material, system or method listed is relevant to your study. If you are not sure if a list item applies to your research, read the appropriate section before selecting a response.

Materials & experimental systems

n/a	Involved in the study
☐	☒ Antibodies
☐	☒ Eukaryotic cell lines
☒	☐ Palaeontology and archaeology
☐	☒ Animals and other organisms
☒	☐ Human research participants
☒	☐ Clinical data
☒	☐ Dual use research of concern

Methods

n/a	Involved in the study
☒	☐ ChIP-seq
☐	☒ Flow cytometry
☒	☐ MRI-based neuroimaging

Antibodies

Antibodies used

Primary antibodies: anti-MMP9 antibody (Abcam ab38898, Lot# 573144), anti-biotin antibody (Abcam ab201341, Lot# GR3232475-1), anti-CAIX antibody (Abcam ab15086, Lot# GR290257-1), anti-FITC antibody (GeneTx GTX19224, Lot# 821300832, for IF); mouse anti-FITC monoclonal antibody Clone 2A3 (GeneTex GTX10257, Lot# 821504362, for ELISA).
Secondary antibodies: Donkey anti-Rabbit IgG (H+L) Highly Cross-Adsorbed Secondary Antibody, Alexa Fluor 647 (ThermoFisher A-31573, Lot# 1322326); Donkey anti-Mouse IgG (H+L) Highly Cross-Adsorbed Secondary Antibody, Alexa Fluor 555 (ThermoFisher A-31570, Lot# 412442); Donkey anti-Goat IgG (H+L) Cross-Adsorbed Secondary Antibody, Alexa Fluor 633 (ThermoFisher A-21082, Lot# 1889311); Donkey anti-Rabbit IgG (H+L) Highly Cross-Adsorbed Secondary Antibody, Alexa Fluor 555 (ThermoFisher A-31572, Lot# 400466).
NeutrAvidin-HRP (ThermoFisher 31030, Lot# RA228784).

Validation

All commercially available antibodies have been thoroughly tested and validated by the manufacture. Validation statements are available on manufacture's website. Specifically:
The Anti-MMP9 antibody (ab38898, https://www.abcam.com/mmp9-antibody-ab38898.html) was shown to bind to the Recombinant Human MMP9, His tagged (ab82955) and also to the Recombinant Mouse MMP9 protein (ab39309) indicating that it is specific for the MMP9 target. ab38898 detects recombinant Human MMP9 running at ~85 kDa, and endogenous full-length MMP9 in LPS-stimulated cells at ~100 kDa. This antibody also detects a band at 90 kDa in U937 PMA-treated cells. Tested applications of the antibody include IHC-Fr, WB. This antibody has been referenced in 602 publications. Selected recent citations:
Qin T et al. J Ethnopharmacol 246:112128 (2020);
Chen X et al. J Exp Clin Cancer Res 39:65 (2020);
Hu L et al. J Gastric Cancer 20:95-105 (2020).

The Anti-Biotin antibody [Hyb-8] (ab201341, https://www.abcam.com/biotin-antibody-hyb-8-ab201341.html) has not been KO tested or tested for specificity using a blocking with immunizing peptide. It is suitable for Flow Cyt, In situ hybridization, WB, ICC/IF, IHC analysis and has been cited in 3 publications:
Shaw A et al. Nat Nanotechnol 14:184-190 (2019);
Powell ML et al. Anal Biochem 543:108-115 (2018);
Roussis IM et al. PLoS One 11:e0147967 (2016).

The Anti-Carbonic Anhydrase 9/CA9 antibody (ab15086, https://www.abcam.com/carbonic-anhydrase-9ca9-antibody-ab15086.html) has been used successfully in 99 publications. Western Blot analysis of the Anti-Carbonic Anhydrase 9/CA9 antibody (ab15086) in HeLa, MDA-MB-231, and A549 whole cell lysates showed a specific band detected for Carbonic Anhydrase IX/CA9 at a molecular weight of 50 kDa. Selected recent citations:
Lorenzo-Pouso AI et al. J Enzyme Inhib Med Chem 35:1258-1266 (2020);
Hart PC et al. Cell Rep 29:4086-4098.e6 (2019);
Dillon MT et al. Clin Cancer Res 25:3392-3403 (2019).

Fluorescein antibody (GTX19224) was generated from monospecific antiserum by immunoaffinity chromatography using Fluorescein conjugated Goat IgG coupled to agarose beads followed by solid phase adsorption(s) to remove any unwanted reactivities. Assay by immunoelectrophoresis resulted in a single precipitin arc against anti-Goat Serum and Fluorescein conjugated Bovine Serum Albumin. Tested applications for the antibody included WB, ICC/IF, ELISA and IHC. Specificity of the anti-FAM antibody was further validated in house using ELISA with a short synthetic peptide labeled with FAM and biotin ligands.
Citation: Lin KY et al. ACS Nano. 7,10, 9001-9009 (2013).

Mouse anti-fluorescein antibody (GTX10257) was tested to react with both free and conjugated FTIC. Immunogen: fluorescein conjugated Bovine Serum Albumin. Antibody was Protein A purified and tested applications for the antibody included ELISA and IHC.
Citations:
Mac, QD et al., Nat Biomed Eng 3, 281-291 (2019);
Holt BA et al., J Vis Exp. (137):57937 (2018);
Warren AD et al., Proc. Natl. Acad. Sci. U.S.A. 111 (10) 3671-3676 (2014).

Eukaryotic cell lines

Policy information about cell lines

Cell line source(s)

Mouse cell lines MC26-LucF (Kenneth K. Tanabe Laboratory, Massachusetts General Hospital), D8-175 KPC-derived pancreatic cancer line (Tyler Jacks Laboratory, Massachusetts Institute of Technology) and 4T1 (ATCC CRL-2539); human cell lines MDA-MB-435 (NCI-60), U937 (ATCC CRL-1593.2), OVCAR8 (NCI-60) and LS174T (ATCC CL-188)

Authentication

The commercially available cell lines from ATCC have been thoroughly tested and authenticated using short tandem repeat profiling by the vendor. Statements are available on vendor's website (https://www.atcc.org/Products/Cells_and_Microorganisms/Testing_and_Characterization/STR_Profiling_Analysis.aspx). Cell line received from other research lab was previously validated upon receipt, references of the cell line were provided.
Selected citations for the MC26-LucF line:
Danino T et al., Sci Transl Med 7, 289, pp. 289ra84 (2015)
Kwon E et al., Nat Biomed Eng 1, 0054 (2017).

Selected citations for the D8-175 line:
Maud-Emmanuelle G et al., Clin Cancer Res 24(7):1734-1747 (2018)
Lo JH et al., Mol Cancer Ther 17(11): 2377–2388 (2018)

Mycoplasma contamination	All cell lines were tested negative for mycoplasma contamination.
Commonly misidentified lines (See ICLAC register)	MDA-MB-435 line was previously described as a metastatic breast cancer cell line, and is now considered a melanoma line. Cell lines were utilized to demonstrate the broad application of the low pH insertion peptide in solid tumors, especially ones with high invasive potential.

Animals and other organisms

Policy information about studies involving animals; ARRIVE guidelines recommended for reporting animal research

Laboratory animals	Female BALB/c mice (Taconic, 6-8 weeks at time of tumor induction) and female NCR Nude mice (Taconic, 4-5 weeks at time of tumor induction) were used in this study. All animals were maintained in the Koch Cancer Institute animal facility, with a 12-h light/12-h dark cycle, at ~18-23°C and ~50% humidity. Complete descriptions can be found in relevant methods and figure legends.
Wild animals	This study did not involve wild animals.
Field-collected samples	This study did not involve samples collected from the field.
Ethics oversight	All animal studies were approved by the Massachusetts Institute of Technology (MIT) committee on animal care (MIT protocol 0417-025-20 & 0217-014-20). All animals received humane care, and all experiments were conducted in compliance with institutional and national guidelines and supervised by Division of Comparative Medicine (DCM) of MIT staff.

Note that full information on the approval of the study protocol must also be provided in the manuscript.

Flow Cytometry

Plots

Confirm that:

☒ The axis labels state the marker and fluorochrome used (e.g. CD4-FITC).

☒ The axis scales are clearly visible. Include numbers along axes only for bottom left plot of group (a 'group' is an analysis of identical markers).

☒ All plots are contour plots with outliers or pseudocolor plots.

☒ A numerical value for number of cells or percentage (with statistics) is provided.

Methodology

Sample preparation	Cells cultured in 6-well tissue culture plates were collected directly from the adherent surface by pipetting with and resuspending in PBS (pH 7.4 or 6.4) and analyzed on a BD LSRII flow cytometer immediately.
Instrument	BD LSR II HTS Flow Cytometer (BD Biosciences)
Software	Data acquisition was performed with FACS Diva Version 8.0 on an LSR II Flow Cytometer. Data were analyzed in FlowJo (TreeStar Software, Version 9.9.6).
Cell population abundance	The signal from 10,000 cells after post-sort fractions were collected and used for further analyses.
Gating strategy	The sub-population of viable cells after standard FSC/SSC gating for uniform population

☒ Tick this box to confirm that a figure exemplifying the gating strategy is provided in the Supplementary Information.